Letter

Gate-tunable ferromagnetism in $Cr_2Si_2Te_6$ thin flakes

Changhong Yuan,[1,2,*] Yutong Wang,[1,2,*] Xu Yan,[1,3,*] Kunya Yang,[4] Wenxin Cheng,[1,2] Yating Jiang,[1,2] Qiuyan Shi,[1,2] Xingyu Jiang,[1] Xuewei Wang,[1,2] Zhiyu Huang,[1,2] Yuhan Jin,[1,2] Beiyi Zhu,[1,2] Jie Yuan,[1,2] Mingquan He,[5,†] Quansheng Wu,[1,2,‡] and Qihong Chen[1,2,§]

[1]*Beijing National Laboratory for Condensed Matter Physics, Institute of Physics, Chinese Academy of Sciences, Beijing 100190, China*
[2]*School of Physical Sciences, University of Chinese Academy of Sciences, Beijing 100049, China*
[3]*College of Physics and Hebei Advanced Thin Films Laboratory, Hebei Normal University, Shijiazhuang, Hebei 050024, China*
[4]*Department of Physics, Chongqing Three Gorges University, Chongqing 404100, China*
[5]*College of Physics & Center of Quantum Materials and Devices, Chongqing University, Chongqing 401331, China*

(Received 13 November 2025; revised 11 February 2026; accepted 16 March 2026; published 9 April 2026)

While intrinsic two-dimensional (2D) ferromagnetic (FM) materials hold great promise for spintronic applications, external control over both electrical and magnetic properties is crucial. Here, we demonstrate effective modulation of electronic and magnetic characteristics of $Cr_2Si_2Te_6$ (CST) through ionic liquid gating (ILG). Upon electron doping via ILG, CST undergoes a semiconductor-to-metal transition, accompanied by remarkable enhancements in Curie temperature (T_c, from 33 K to 110 K) and coercive field (H_c, from 1.4 mT to 50 mT). Moreover, under high doping levels, the magnetic easy axis can be electrically switched from the out-of-plane to the in-plane direction. Theoretical calculations suggest a possible scenario in which electron doping strengthens FM coupling through a double-exchange mechanism between mixed-valence Cr ions, thereby boosting T_c. These findings highlight ILG as a versatile strategy for tailoring magnetism in 2D ferromagnets and offering pathways for next-generation spintronic devices.

DOI: 10.1103/nlt7-52tc

Introduction. Since the discovery of graphene [1], two-dimensional (2D) materials have attracted tremendous attention owing to their extraordinary physical properties and broad potential for applications [2–4]. Among them, the emergence of intrinsic 2D ferromagnetic (FM) materials has not only opened new avenues for exploring low-dimensional magnetism, but also created unprecedented opportunities for next-generation device technologies [5–8]. Prototypical examples such as $Cr_2Ge_2Te_6$ (CGT), CrI_3, and Fe_3GeTe_2 have been demonstrated to maintain long-range FM order in few-layer or even monolayer limits at finite temperatures, enabled by pronounced magnetic anisotropy [6–8]. This not only overcomes the constraints imposed by the Mermin-Wagner theorem, but also provides an ideal experimental platform for the precise investigation of the intricate coupling among spin, charge, orbital, and lattice degrees of freedom. From an application perspective, FM semiconductors integrate the functionalities of both semiconductors and ferromagnets, which enable electrical control of electron charge and spin and thus constitute a compelling platform for high-performance, low-power spintronic devices [9,10].

Compared to their bulk counterparts, thin flakes of ferromagnets are more susceptible to manipulation by multiple external knobs, including electric field [8,11], magnetic field [12], and pressure [13]. Among these approaches, ionic liquid gating (ILG) has emerged as a powerful technique for *in situ* modulation of carrier concentration ($10^{14} \sim 10^{15}\,cm^{-2}$) or ion doping [8,14–17]. Beyond electrical property, this approach enables effective control over magnetic properties of 2D FM materials, such as Curie temperature (T_c), coercive field (H_c), saturation magnetization, and magnetic easy axis orientation [8,11,18]. For instance, in the FM semiconductor CGT, ILG induces a semiconductor-to-metal transition accompanied by an enhancement of T_c and a reorientation of the magnetic easy axis [11], establishing an excellent platform for exploring emergent quantum phenomena via electric-field control within a single device.

$Cr_2Si_2Te_6$ (CST), an isostructural analogue of CGT, belongs to the same family of transition-metal trichalcogenides and is likewise a FM semiconductor with high electrical resistivity [19]. It exhibits strong magnetic anisotropy featuring an out-of-plane easy axis and retains FM order down to the monolayer limit [20,21]. Optical studies reveal that CST possesses a narrower band gap [22,23], a lower T_c, and weaker spin-orbit coupling compared to CGT, and yet with pronounced spin-lattice coupling [22], making it highly responsive to external perturbations such as doping or strain. While back-gate modulation using a SiO_2 dielectric layer can slightly improve the conductivity of CST, its intrinsic semiconducting behavior remains largely unaltered [24]. In contrast, theoretical calculations predict that high levels of electron doping can drive a semiconductor-to-metal transition in CST [25,26]. This prediction has been experimentally verified under high pressure [27], where a further increase in electron concentration leads to superconductivity.

*These authors contributed equally to this work.
†Contact author: mingquan.he@cqu.edu.cn
‡Contact author: quansheng.wu@iphy.ac.cn
§Contact author: qihongchen@iphy.ac.cn

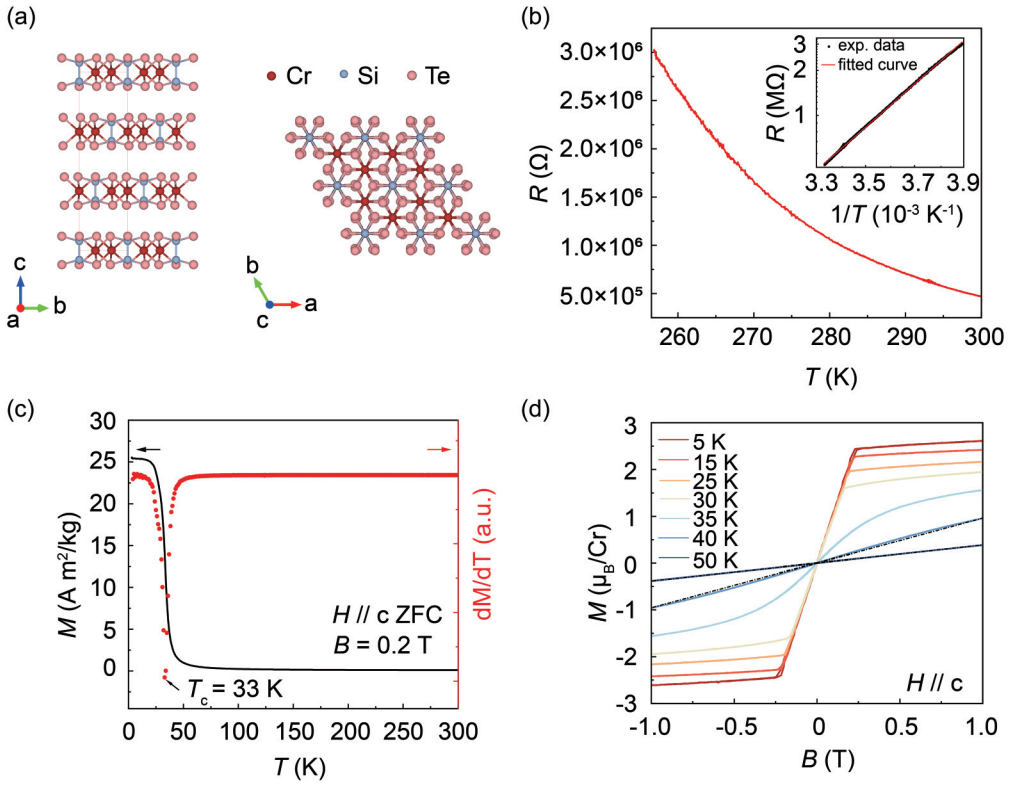

FIG. 1. Crystal structure, transport properties, and magnetic properties of bulk $Cr_2Si_2Te_6$ (CST). (a) Schematics of the crystal structure of CST viewed from *a*-axis (left) and *c*-axis (right) directions. The rectangle outlines the unit cell. (b) Temperature-dependent resistance of bulk CST. Inset: Resistance data fitted with the thermal activation model. (c) Temperature-dependent magnetic susceptibility of bulk CST and corresponding derivative under zero-field cooling (ZFC) mode with a magnetic field of 0.2 T applied along the *c* axis. (d) Isothermal magnetization measurements at different temperatures of bulk CST. Dashed lines are linear guidelines.

Nevertheless, reports on the evolution of the FM order under pressure have not always been consistent [28]. Beyond pressure tuning, systematic exploration of how carrier doping influences both the electronic and magnetic properties of CST is essential for clarifying the origin of its magnetism as well as advancing its potential in device applications.

In this work, we demonstrate that the electrical and magnetic properties of CST flakes can be effectively tuned through electron doping via ILG. Upon doping, CST undergoes a semiconductor-to-metal transition, accompanied by a remarkable increase in T_c from 33 K to 110 K, and a rise in H_c from 1.4 mT to 50 mT. At high doping levels, the magnetic easy axis reorients from the out-of-plane to the in-plane direction. Theoretical analysis indicates that the enhancement of T_c arises from doping-induced modifications of the FM exchange interaction.

Results and discussion. As shown in Fig. 1(a), CST crystallizes in a rhombohedral structure (space group $R\bar{3}$), which is composed of vertically stacked Te–(Cr/Si)–Te layers. Within each layer, the Cr^{3+} ions are octahedrally coordinated by six neighboring Te atoms and collectively form a nearly ideal honeycomb lattice. Figure 1(b) displays the temperature-dependent resistance of bulk CST, which shows typical semiconducting behavior. As shown in the inset, an energy gap of 0.58 eV is extracted from the thermal activation model $R = R_0 \exp\left(\frac{E_g}{2k_B T}\right)$, where the fitting is restricted to the high-temperature regime in which reliable resistance data can be obtained. Despite the limited temperature range, the extracted E_g agrees well with the optical measurements and theoretical calculations [22,29]. Figure 1(c) shows the temperature-dependent magnetic susceptibility of bulk CST and its derivative, revealing a T_c of 33 K, consistent with previous reports [22,27,28,30]. Figure 1(d) displays the isothermal magnetization curves at different temperatures. The negligible hysteresis below T_c and the ultralow H_c of only 1.4 mT at 5 K demonstrate the soft FM nature of CST. In the temperature range slightly above T_c (35–40K), the magnetization curves deviate from the linear paramagnetic response observed at 50 K and exhibit a clear low-field nonlinearity without hysteresis, which becomes more pronounced closer to T_c, particularly at 35 K. Such low-field nonlinearity of the magnetization curves above T_c, together with the absence of hysteresis, is suggestive of short-range magnetic correlations, where spins may form correlated regions that respond collectively to an external magnetic field despite the absence of long-range FM order.

To achieve efficient and homogeneous gating effect, ILG was performed on exfoliated thin flakes. Due to the thermal instability of CST flakes [31], a transfer method onto predefined electrodes was adopted to avoid heat-induced degradation during electron-beam lithography. An optical microscopy image of sample No. 1 (denoted as S1) is presented in Fig. 2(a), with a thickness of approximately 40 nm estimated by the optical contrast method [31]. As indicated in Fig. 2(b), the flake maintains bulklike semiconducting behavior. Figure 2(a) also illustrates the schematic of the ILG

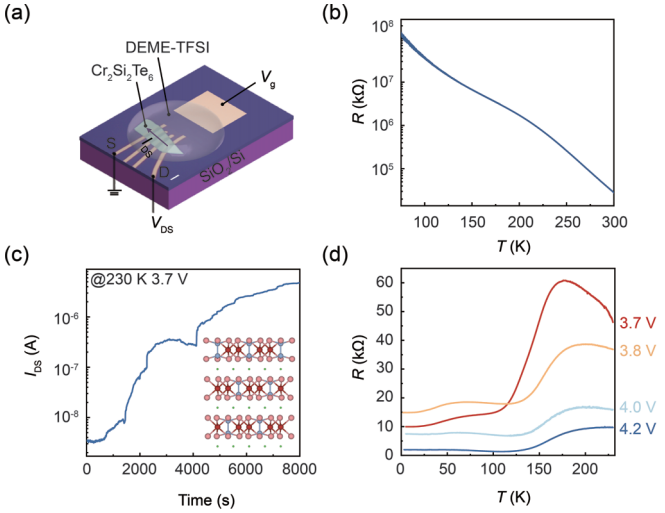

FIG. 2. Electrical transport properties of sample S1 with ionic liquid gating (ILG). (a) Schematic of CST device (S1) with ILG. Scale bar: 5 μm. (b) Temperature-dependent resistance of S1 in its pristine state (before gating) using the two-probe method. (c) I_{DS} versus time curve for S1 at $T = 230$ K under $V_g = 3.7$ V, with $V_{DS} = 0.5$ V. Inset: Crystal structure of CST intercalated by H^+ ions. (d) Temperature-dependent resistance for S1 gated at 230 K under different V_g of 3.7, 3.8, 4.0, and 4.2 V.

device, where a droplet of ionic liquid (DEME-TSFI) serves as the dielectric, simultaneously covering the sample surface and the gate electrode.

Generally, ILG can operate in two different regimes: electrostatic gating and electrochemical gating. As reported in previous studies [43], DEME-TFSI exhibits electrostatic effect when the gating temperature (T_g) is lower than 220 K, while electrochemical effects may arise at higher temperatures. For a purely electrostatic gating scenario, a high-density charge accumulation layer is confined to a near-surface region with a thickness of only a few nanometers due to electrostatic screening, resulting in a surface-limited modulation [14,44]. In contrast, electrochemical gating can drive ions into or out of the sample. In layered 2D materials, ionic diffusion (small ionic species, such as H^+ and Li^+) can proceed both laterally along interlayer spacings from the edges and vertically from the top surface into the bulk [45]. In this scenario, the modulation depth is governed by ionic diffusion. Previous studies on FeSe have demonstrated that electrochemical gating can achieve spatially uniform bulk modulation in samples with lateral dimensions on the order of millimeters and thicknesses of up to ∼200 nm [46]. Therefore, it is plausible to infer that the vertical diffusion depth is on the order of hundreds of nanometers. Consequently, electrochemical gating can induce bulklike modulation in samples with appropriate dimensions.

In our experiments, electrostatic gating ($T_g = 220$ K) produced no observable change in the resistivity of CST (see Fig. S3 in Supplemental Material) [31], unlike the observation in CGT [11]. Consequently, we employed electrochemical gating ($T_g = 230$ K), which offers stronger modulation capability. Both theoretical calculations and experimental studies indicate that electron doping reduces the resistivity of CST, driving a semiconductor-to-metal transition [25–28]. To achieve this, a positive gate voltage (V_g) was applied, which drive cations (primarily H^+ ions originating from the unavoidable water molecules in the ionic liquid) into the sample [46,47], thereby increasing the electron density [inset of Fig. 2(c)]. Figure 2(c) presents the drain-source current (I_{DS}) versus time for S1 at 230 K under $V_g = 3.7$ V. Under these conditions, I_{DS} increases by three orders of magnitude, from 3.4×10^{-9} A to 4.7×10^{-6} A, before saturating, demonstrating a pronounced reduction in electrical resistance.

Figure 2(d) displays the temperature-dependent resistance (R-T) curves of S1 gated at 230 K under different V_g. All curves exhibit a similar trend of resistance drop with decreasing temperature, signifying metallic transport. At lower V_g values, for example $V_g = 3.7$ V, a slight increase of resistance appears around 200 K upon cooling. This semiconductor-like behavior likely arises from an incomplete transition to a metallic state. As V_g increases and additional electrons are introduced, the overall resistance systematically decreases. At $V_g = 4.2$ V, the semiconductorlike upturn near 200 K becomes nearly invisible, and the resistance decreases with cooling, reflecting enhanced metallicity. Interestingly, the resistance evolution under ILG closely resembles the electrical properties of bulk CST under hydrostatic pressure, where superconductivity with a critical temperature of ∼4.5 K has been reported [27]. However, no signs of superconductivity were observed down to 2 K in our experiments, possibly due to the absence of the structural transition, which takes place in pressure-tuning experiments [27,29]. It should be noted that when the applied V_g is higher than 4.2 V, the sample resistance begins to rise; however, it decreases again when V_g is reduced, confirming the reversibility of the gating process and ruling out chemical etching effects as the cause of resistance rise (Fig. S4) [31]. This behavior likely stems from enhanced disorder in the heavily doped regime: as more ions are injected, the disorder effect progressively dominates over the carrier concentration tuning, leading to higher resistance. This interpretation is supported by experiments in which lithium ions were added to the ionic liquid—due to their larger ionic radius, lithium intercalation introduces stronger disorder into CST, and consequently the sample resistance shows a significant decrease, but metallic behavior fails to emerge (Fig. S5) [31].

To probe the magnetic state, we systematically measured the magnetoresistance (MR) of S1 under 3.8 V V_g with out-of-plane magnetic field, over the temperature range of 2–170 K. MR is defined as $\mathrm{MR} = \frac{R(H)-R(0)}{R(0)} \times 100\%$. The magnetic field at which the MR peak occurs corresponds to H_c. As shown in Fig. 3(a), a pronounced MR hysteresis loop is observed at 5 K with $H_c = 50$ mT, representing a 36-fold enhancement compared to pristine bulk CST. With increasing temperature, H_c decreases gradually to zero, as shown in Fig. 3(d). Butterfly-shaped MR hysteresis loops, a hallmark of FM order, are present in the range of 2–110 K, and disappear completely above 130 K. Therefore, T_c lies between 110 and 130 K, nearly three times higher than that of bulk CST. This trend is consistent with pressure-driven enhancements of both T_c and H_c in CST bulk and flake [13,28].

Additional MR measurements were performed on another sample (S2) under different gating conditions (Figs. S6–S8)

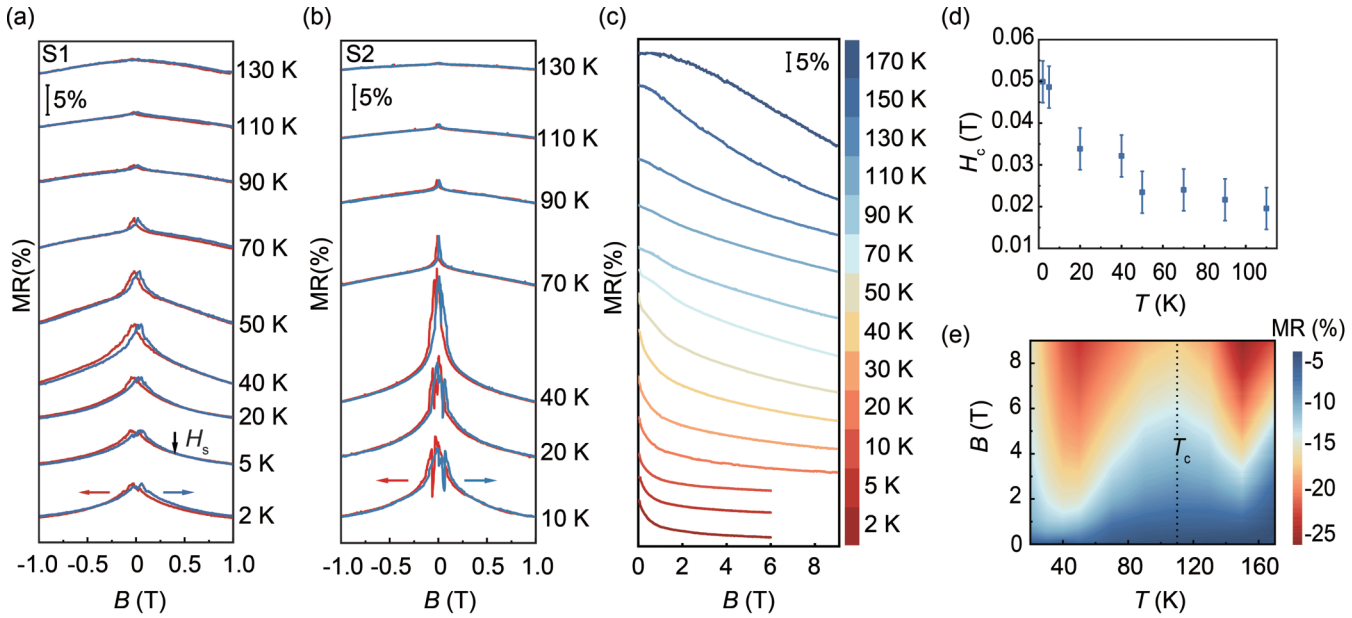

FIG. 3. Magnetic properties of S1 under $V_g = 3.8$ V and S2 under $V_g = 4.5$ V, H // c. (a) Magnetic field-dependent MR of S1 at different temperatures. The MR curves are vertically shifted for clarity. The blue and red arrows denote the forward and backward sweep of magnetic field, respectively. The black arrow marks the saturation field (H_s) at 5 K, where the resistance hysteresis disappears. (b) Magnetic field-dependent MR of S2 at different temperatures. (c) Magnetic field-dependent MR of S1 at different temperatures in a higher field range. (d) Coercive field (H_c) of S1 as a function of temperature. Error bars represent the systematic error in determining H_c. (e) Contour plot of MR as a function of temperature and magnetic field [same data as in Fig. 3(c)].

[31], where similar behavior was observed. Notably, T_c remains consistently within 110–130 K regardless of electron doping level (Fig. S7) [31], suggesting that T_c essentially reaches saturation once metallic behavior emerges. Besides the negative magnetoresistance (N-MR), S2 exhibits positive magnetoresistance (P-MR) at low temperatures and weak magnetic fields in the FM state, as shown in Fig. 3(b). When an in-plane magnetic field is applied, the P-MR observed under out-of-plane field disappears (Fig. S9) [31]. This behavior can be attributed to the switching of the magnetic easy axis from the out-of-plane to the in-plane configuration [48]. When the out-of-plane field reorients the spins from perpendicular to parallel alignment with respect to the field, the resistance increases, giving rise to P-MR. In addition, Figs. 4(a) and 4(b) show the out-of-plane and in-plane hysteresis loops of sample S7 at 60 K. To extract the saturation field (H_s) more intuitively, we plot the difference between the two resistance-field curves obtained from backward and forward magnetic-field sweeps, $\Delta R = R(B-) - R(B+)$, as shown in Figs. 4(c) and 4(d). H_s corresponds to the magnetic field at which the difference ΔR becomes negligible. The smaller H_s observed for the in-plane direction suggests that the easy-axis lies in the plane. The P-MR feature is not evident in S1, which may be attributed to the weaker gating strength and the lower doping level, and the magnetic easy axis likely remains oriented out of plane. The tunability of magnetic anisotropy by gating demonstrates electrical control of magnetization orientation in CST.

The magnetic state is further reflected in the magnitude of MR as a function of magnetic field and temperature [Fig. 3(c)]. Although N-MR persists across the entire temperature range from 2 K to 170 K, the field dependence of MR exhibits a pronounced temperature dependent evolution. At low temperatures (2–110 K), MR drops sharply at low fields and tends to saturate at high fields, giving a concave profile. Above 110 K, MR shows a much smoother decrease across the entire field range, resulting in a convex profile. The concave-to-convex transition temperature coincides with T_c, implying distinct physical origins of N-MR below and above the FM ordering temperature. This change is clearly visualized in the contour plot as shown in Fig. 3(e), which highlights the variation of the magnitude of N-MR across T_c.

These results indicate the coexistence of multiple mechanisms governing N-MR in CST. In the FM state, magnetic field can align the magnetic moments into a more ordered configuration, thereby reducing electron-spin scattering. MR saturates once the magnetic field reaches H_s, which in 2D FM materials is generally a few tenths of a tesla [11,18,48]. In ion-gated CST, H_s (defined as the field at which the resistance hysteresis disappears) is approximately 0.4 T at 5 K—slightly higher than the bulk value of 0.25 T—consistent with the sharp resistance drop at low fields. High-pressure studies on CST flakes likewise show that H_s remains small after metallization, not exceeding 0.2 T at 16 K [13]. Above T_c, the persistence of N-MR likely stems from short-range FM correlations, which have been reported to survive within the *ab* plane up to at least 300 K [49].

To elucidate the underlying mechanisms responsible for the remarkable enhancement of T_c, H_c, and the magnetic easy axis reorientation, we have performed first-principle calculations to track the evolution of electronic and magnetic structures in CST under electron doping. The detailed calculation procedures and results are provided in the Methods and Figs. S10–S13 [31]. The doping level is parametrized by η, defined as the number of doped electrons per $Cr_2Si_2Te_6$ formula

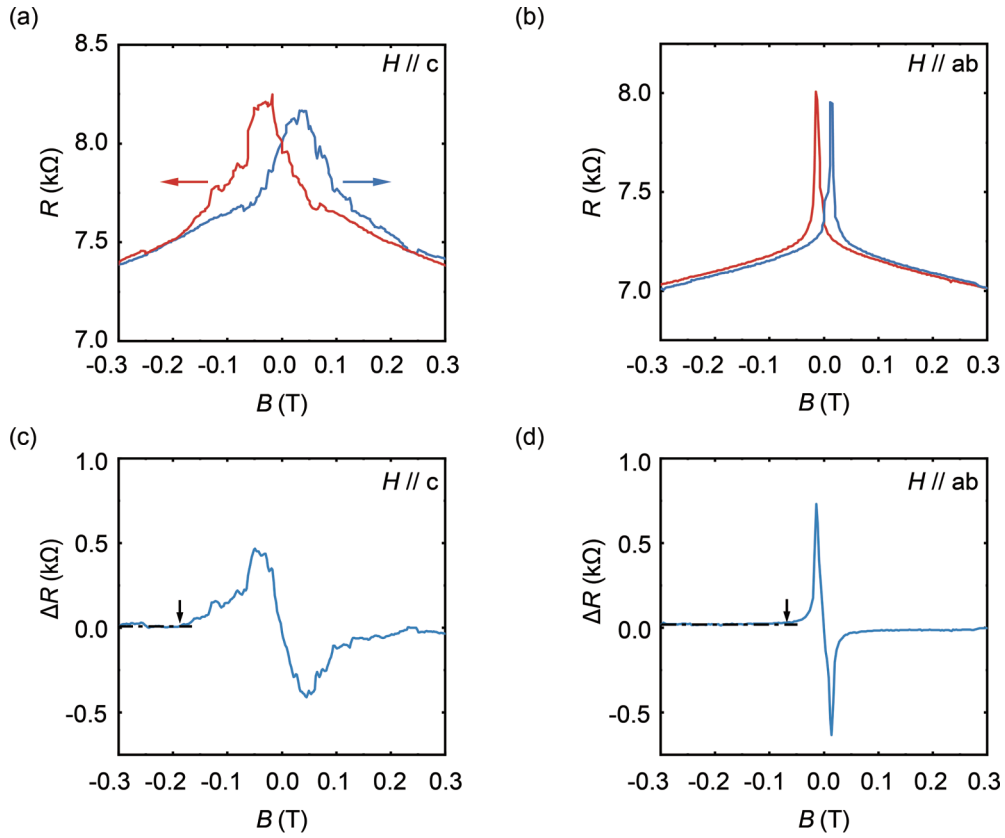

FIG. 4. The (a) out-of-plane and (b) in-plane hysteresis loops of sample S7 at 60 K. (c), (d) The difference between the two resistance-field curves obtained from backward and forward magnetic-field sweeps, $\Delta R = R(B-) - R(B+)$. The black arrow marks H_s, where the difference ΔR becomes negligible. Panels (c) and (d) correspond to field applied perpendicular and parallel to the *ab* plane, respectively.

unit (/f.u.). The magnetic anisotropy energy (MAE) is defined as the total energy difference between the out-of-plane ⟨001⟩ and the in-plane ⟨100⟩ magnetization directions. Figure 5(a) presents the calculated dependence of T_c and MAE on electron doping η. For pristine CST ($\eta = 0$), T_c estimated within the mean-field approximation is 25 K, close to the experimental value. The negative MAE value of -0.142 meV/Cr indicates enhanced stability of the out-of-plane spin orientation relative to the in-plane configuration, consistent with previous reports [20,21]. With increasing doping concentration η, both T_c and MAE rise monotonically: T_c increases from 25 K to 78 K, exhibiting a tendency toward saturation. The enhancement of MAE could result in an increased H_c. Notably, the MAE changes sign from negative to positive, indicating an easy axis reorientation to the in-plane direction. These results show qualitative agreement with the experimental observations.

Figures 5(c)–5(f) show atom-resolved and Cr orbital-resolved projected density of states (PDOS) of pristine and doped CST ($\eta = 0.25$). Pristine CST exhibits semiconducting characteristics, with the conduction band minimum (CBM) and valence band maximum (VBM) primarily contributed by Cr d and Te p orbitals, respectively. The obtained indirect band gap of 0.54 eV is comparable to the activation energy obtained from the temperature dependence of resistivity. As shown in Fig. 5(b), the indirect superexchange interaction mediated through Cr-Te-Cr pathways where the bond angle is close to 90°, dominates the weak FM coupling between neighbor Cr ions as described by the Goodenough-Kanamori-Anderson (GKA) rules. With electron doping, the Fermi level shifts progressively toward the CBM, driving a semiconductor-to-metal transition (Fig. S10) [31]. The added electrons primarily occupy the Cr d_{xz} and d_{yz} orbitals as itinerant carriers, contributing to electrical conduction. The metallic behavior and significant enhancement of T_c under electron doping, along with the modification in the valence state of the Cr ions, indicate that the exchange interaction is unlikely to be dominated by superexchange interaction, which requires electrons to be localized. The magnetism of electron-doped CST favors mechanisms typical of metallic ferromagnets, such as itinerant electron exchange or double exchange. Indeed, the reduction of resistance near T_c mirrors that of doped rare-earth manganites (e.g., $La_{1-x}Sr_xMnO_3$) [50,51], suggesting that the two systems may share a common mechanism—the double-exchange interaction. This interaction is demonstrated in metallic systems with magnetic ions in mixed valence states. As shown in Fig. 5(b), a portion of Cr^{3+} ions is reduced to Cr^{2+} after doping and the preserved spin hopping of itinerant electrons across Cr^{2+}−Te−Cr^{3+} pathways generates the double-exchange interaction. This mechanism accounts for both the metallic conduction and the remarkable enhancement of T_c observed in doped CST.

It is instructive to compare the results with previous ionic gating studies on the isostructural compound CGT. Although pristine CST and CGT exhibit substantially different T_c values, both systems exhibit a similar ∼threefold enhancement in T_c under ionic gating. Moreover, similar gating-induced

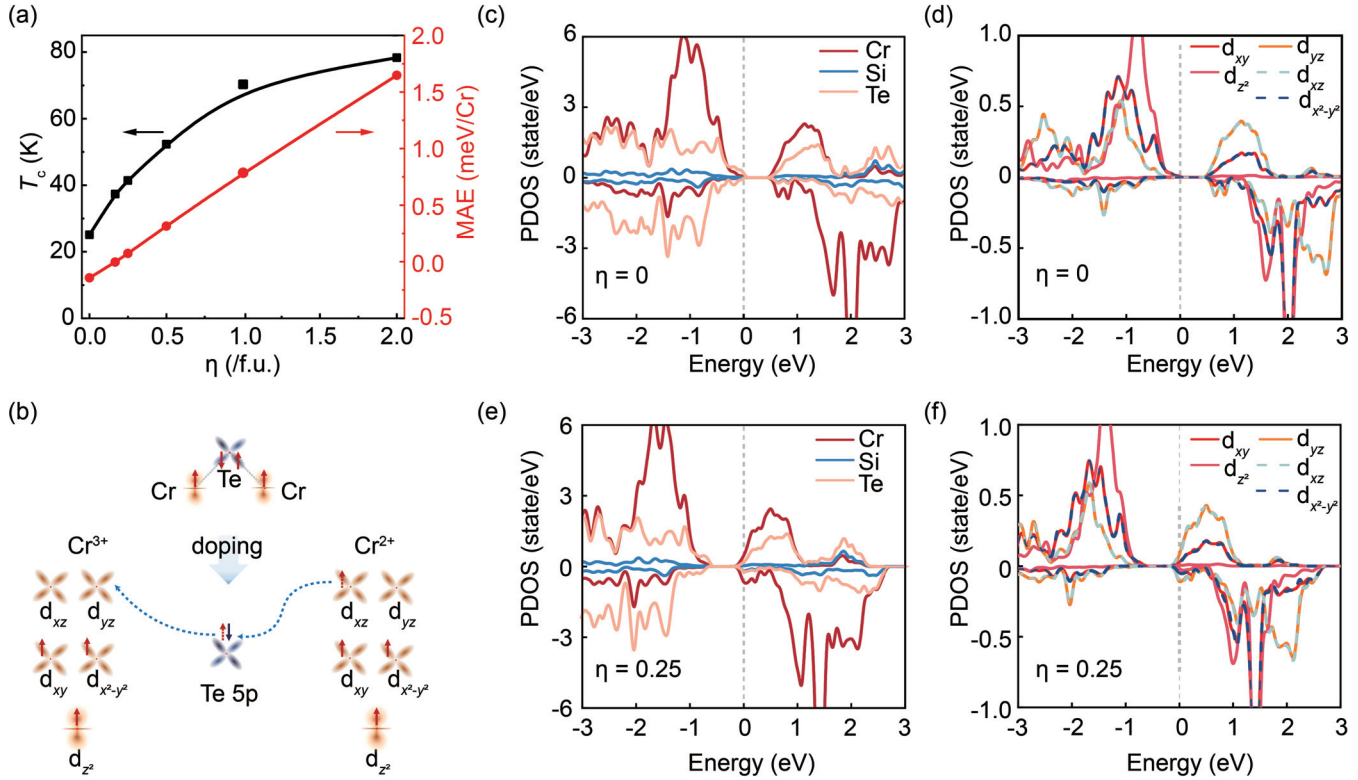

FIG. 5. Evolution of magnetic properties and electronic structure with electron doping in CST. (a) The calculated dependence of T_c and MAE on η. η represents the number of electrons doped per $Cr_2Si_2Te_6$ formula unit. (b) Schematic diagrams of the superexchange interaction in pristine CST and the double-exchange interaction in gated CST. (c)–(f) Atomic-resolved and Cr orbital-resolved projected density of states (PDOS) of pristine (c), (d) and doped CST with $\eta = 0.25$ (e), (f).

phenomena, such as the semiconductor-to-metal transition and the reorientation of the magnetic easy axis, are observed in both materials. These similarities suggest that the enhancement of ferromagnetism under ionic gating is governed by a common physical mechanism. A plausible scenario is that electron doping modifies the dominant magnetic exchange interactions in both compounds. Upon sufficient electron doping, the increased carrier density and the accompanying changes in orbital occupancy can enhance carrier-mediated exchange processes, thereby effectively strengthening the FM coupling and leading to a pronounced increase in T_c. Within this picture, the similar relative enhancement of T_c in both materials can be attributed to a comparable fractional strengthening of the effective FM exchange.

Conclusion. In summary, we have shown that ILG can effectively modulate the electronic and magnetic properties of CST flakes via electron doping. The semiconductor-to-metal transition, significant enhancement of T_c and H_c, and the magnetic easy axis reorientation collectively illustrate the strong coupling between charge carriers and magnetic order. One plausible interpretation is that the enhanced ferromagnetism originates from a double-exchange mechanism mediated by itinerant electrons in Cr d orbitals, which replaces the superexchange interaction governing the undoped semiconducting state. These results not only highlight the potential of ionic gating for manipulating magnetic states in 2D FM semiconductors, but also deepen our understanding of carrier-dependent magnetism in correlated electron systems.

Acknowledgments. The authors would like to thank Xiaoli Dong, Hua Zhang, Zuxiu Guo, and Chang Liu for their assistance with the magnetization measurements. This work was supported by the National Natural Science Foundation of China (Grants No. 12374141, No. 12274436, and No. 12474141); the National Key Basic Research Program of China (Grants No. 2022YFA1403900 and No. 2022YFA1403000); the Chinese Academy of Sciences President's International Fellowship Initiative (Grant No. 2024DM0018); the Open Research Fund of the Pulsed High Magnetic Field Facility (Grant No. WHMFC2024001), Huazhong University of Science and Technology; the Open Fund of the China Spallation Neutron Source Songshan Lake Science City (Grant No. KFKT2023B07); the Natural Science Foundation of Chongqing, China (Grant No. CSTB2025NSCQ-GPX0729); the Venture and Innovation Support Program for Chongqing Overseas Returnees (Grant No. cx2024007); and Chinesisch-Deutsche Mobilitätsprogamm of Chinesisch-Deutsche Zentrum für Wissenschaftsförderung (Grant No. M-0496).

Data availability. The data that support the findings of this article are not publicly available. The data are available from the authors upon reasonable request.

[1] K. S. Novoselov, A. K. Geim, S. V. Morozov, D. Jiang, Y. Zhang, S. V. Dubonos, I. V. Grigorieva, and A. A. Firsov, Electric field effect in atomically thin carbon films, Science **306**, 666 (2004).

[2] A. K. Geim and K. S. Novoselov, The rise of graphene, Nat. Mater. **6**, 183 (2007).

[3] K. F. Mak, K. L. McGill, J. Park, and P. L. McEuen, The valley Hall effect in MoS_2 transistors, Science **344**, 1489 (2014).

[4] F. Xia, T. Mueller, Y. Lin, A. Valdes-Garcia, and P. Avouris, Ultrafast graphene photodetector, Nat. Nanotechnol. **4**, 839 (2009).

[5] T. Song, X. Cai, M. W.-Y. Tu, X. Zhang, B. Huang, N. P. Wilson, K. L. Seyler, L. Zhu, T. Taniguchi, K. Watanabe, *et al.*, Giant tunneling magnetoresistance in spin-filter van der Waals heterostructures, Science **360**, 1214 (2018).

[6] B. Huang, G. Clark, E. N. Moratalla, D. R. Klein, R. Cheng, K. L. Seyler, D. Zhong, E. Schmidgall, M. A. McGuire, D. H. Cobden, *et al.*, Layer-dependent ferromagnetism in a van der Waals crystal down to the monolayer limit, Nature (London) **546**, 270 (2017).

[7] C. Gong, L. Li, Z. Li, H. Ji, A. Stern, Y. Xia, T. Cao, W. Bao, C. Wang, Y. Wang, *et al.*, Discovery of intrinsic ferromagnetism in two-dimensional van der Waals crystals, Nature (London) **546**, 265 (2017).

[8] Y. Deng, Y. Yu, Y. Song, J. Zhang, N. Z. Wang, Z. Sun, Y. Yi, Y. Z. Wu, S. Wu, J. Zhu, *et al.*, Gate-tunable room-temperature ferromagnetism in two-dimensional Fe_3GeTe_2, Nature (London) **563**, 94 (2018).

[9] Y. Guo, B. Wang, X. Zhang, S. Yuan, L. Ma, and J. Wang, Magnetic two-dimensional layered crystals meet with ferromagnetic semiconductors, InfoMat **2**, 639 (2020).

[10] W. Jin, G. Zhang, H. Wu, L. Yang, W. Zhang, and H. Chang, Development of intrinsic room-temperature 2D ferromagnetic crystals for 2D spintronics, Chin. Phys. Lett. **40**, 057301 (2023).

[11] I. A. Verzhbitskiy, H. Kurebayashi, H. Cheng, J. Zhou, S. Khan, Y. P. Feng, and G. Eda, Controlling the magnetic anisotropy in $Cr_2Ge_2Te_6$ by electrostatic gating, Nat. Electron. **3**, 460 (2020).

[12] N. P. Wilson, K. Lee, J. Cenker, K. Xie, A. H. Dismukes, E. J. Telford, J. Fonseca, S. Sivakumar, C. Dean, T. Cao, *et al.*, Interlayer electronic coupling on demand in a 2D magnetic semiconductor, Nat. Mater. **20**, 1657 (2021).

[13] C. Zhang, Y. Gu, L. Wang, L. L. Huang, Y. Fu, C. Liu, S. Wang, H. Su, J. W. Mei, X. Zou, *et al.*, Pressure-enhanced ferromagnetism in layered $CrSiTe_3$ flakes, Nano Lett. **21**, 7946 (2021).

[14] Q. H. Chen, J. M. Lu, L. Liang, O. Zheliuk, A. Ali, P. Sheng, and J. T. Ye, Inducing and manipulating heteroelectronic states in a single MoS_2 thin flake, Phys. Rev. Lett. **119**, 147002 (2017).

[15] Q. Chen, J. Lu, L. Liang, O. Zheliuk, A. Ali, and J. Ye, Continuous low-bias switching of superconductivity in a MoS_2 transistor, Adv. Mater. **30**, 1800399 (2018).

[16] R. Zhang, M. Qin, C. Li, Z. Zhao, Z. Wei, J. Xu, X. Jiang, W. Cheng, Q. Shi, X. Wang, *et al.*, Correlation between unconventional superconductivity and strange metallicity revealed by operando superfluid density measurements, Sci. Adv. **11**, eadu0795 (2025).

[17] X. Wei, H. B. Li, Q. Zhang, D. Li, M. Qin, L. Xu, W. Hu, Q. Huan, L. Yu, J. Miao, *et al.*, A selective control of volatile and non-volatile superconductivity in an insulating copper oxide via ionic liquid gating, Sci. Bull. **65**, 1607 (2020).

[18] Z. Wang, T. Zhang, M. Ding, B. Dong, Y. Li, M. Chen, X. Li, J. Huang, H. Wang, X. Zhao, *et al.*, Electric-field control of magnetism in a few-layered van der Waals ferromagnetic semiconductor, Nat. Nanotechnol. **13**, 554 (2018).

[19] N. Ito, T. Kikkawa, J. Barker, D. Hirobe, Y. Shiomi, and E. Saitoh, Spin Seebeck effect in the layered ferromagnetic insulators $CrSiTe_3$ and $CrGeTe_3$, Phys. Rev. B **100**, 060402 (2019).

[20] Z. Zhang, Z. Wang, and Z. Zhang, Magneto-transport and weak anti-localization in ferromagnetic semiconductor $CrSiTe_3$ single crystal, Appl. Phys. Lett. **113**, 142404 (2018).

[21] R. Fujita, J. Liu, X. Hou, Y. Guo, J. Herrero-Martín, G. Van Der Laan, and T. Hesjedal, X-ray spectroscopy for the magnetic study of the van der Waals ferromagnet $CrSiTe_3$ in the few- and monolayer limit, 2D Mater. **9**, 045007 (2022).

[22] L. D. Casto, A. J. Clune, M. O. Yokosuk, J. L. Musfeldt, T. J. Williams, H. L. Zhuang, M. W. Lin, K. Xiao, R. G. Hennig, B. C. Sales, *et al.*, Strong spin-lattice coupling in $CrSiTe_3$, APL Mater. **3**, 041515 (2015).

[23] H. Ji, R. A. Stokes, L. D. Alegria, E. C. Blomberg, M. A. Tanatar, A. Reijnders, L. M. Schoop, T. Liang, R. Prozorov, K. S. Burch, *et al.*, A ferromagnetic insulating substrate for the epitaxial growth of topological insulators, J. Appl. Phys. **114**, 114907 (2013).

[24] M. W. Lin, H. L. Zhuang, J. Yan, T. Z. Ward, A. A. Puretzky, C. M. Rouleau, Z. Gai, L. Liang, V. Meunier, B. G. Sumpter, *et al.*, Ultrathin nanosheets of $CrSiTe_3$: A semiconducting two-dimensional ferromagnetic material, J. Mater. Chem. C **4**, 315 (2016).

[25] X. Liu, Z. Y. Wang, D. Y. Liu, and L. J. Zou, Enhancement of Curie temperature and reorientation of spin in doped $Cr_2Si_2Te_6$, AIP Adv. **11**, 095002 (2021).

[26] X. Li and J. Yang, $CrXTe_3$ (X = Si, Ge) nanosheets: Two dimensional intrinsic ferromagnetic semiconductors, J. Mater. Chem. C **2**, 7071 (2014).

[27] W. Cai, H. Sun, W. Xia, C. Wu, Y. Liu, H. Liu, Y. Gong, D. X. Yao, Y. Guo, and M. Wang, Pressure-induced superconductivity and structural transition in ferromagnetic $CrSiTe_3$, Phys. Rev. B **102**, 144525 (2020).

[28] Y. Lee, C. B. Park, M. Diware, J. Yan, S. Kang, J. Yu, J. Kim, and K. H. Kim, Pressure-induced large anomalous Hall effects in a layered ferromagnet $CrSiTe_3$, npj 2D Mater. Appl. **9**, 45 (2025).

[29] X. Pan, B. Xin, H. Zeng, P. Cheng, T. Ye, D. Yao, E. Xue, J. Ding, and W. H. Wang, Pressure-induced structural phase transition and enhanced interlayer coupling in two-dimensional ferromagnet $CrSiTe_3$, J. Phys. Chem. Lett. **14**, 3320 (2023).

[30] W. Niu, X. Zhang, W. Wang, J. Sun, Y. Xu, L. He, W. Liu, and Y. Pu, Probing the atomic-scale ferromagnetism in van der Waals magnet $CrSiTe_3$, Appl. Phys. Lett. **119**, 172402 (2021).

[31] See Supplemental Material at http://link.aps.org/supplemental/10.1103/nlt7-52tc for details of the experimental methods and theoretical calculations, additional transport data, and calculation results, which includes Refs. [32–42].

[32] K. Yang, H. Wu, Z. Li, C. Ran, X. Wang, F. Zhu, X. Gong, Y. Liu, G. Wang, L. Zhang, *et al.*, Spin-phonon scattering-induced low thermal conductivity in a van der waals layered ferromagnet $Cr_2Si_2Te_6$, Adv. Funct. Mater. **33**, 2302191 (2023).

[33] Y. Liu, W. Wang, H. Lu, Q. Xie, L. Chen, H. Yin, G. Cheng, and X. Wu, The environmental stability characterization of exfoliated few-layer $CrXTe_3$ (X = Si, Ge) nanosheets, Appl. Surf. Sci. **511**, 145452 (2020).

[34] G. Kresse and J. Furthmüller, Efficient iterative schemes for *ab initio* total-energy calculations using a plane-wave basis set, Phys. Rev. B **54**, 11169 (1996).

[35] J. P. Perdew, K. Burke, and M. Ernzerhof, Generalized gradient approximation made simple, Phys. Rev. Lett. **77**, 3865 (1996).

[36] P. E. Blöchl, Projector augmented-wave method, Phys. Rev. B **50**, 17953 (1994).

[37] S. Grimme, Semiempirical GGA-type density functional constructed with a long-range dispersion correction, J. Comput. Chem. **27**, 1787 (2006).

[38] V. Wang, N. Xu, J. C. Liu, G. Tang, and W. T. Geng, VASPKIT: A user-friendly interface facilitating high-throughput computing and analysis using VASP code, Comput. Phys. Commun. **267**, 108033 (2021).

[39] L. Liu, X. Ren, J. Xie, B. Cheng, W. Liu, T. An, H. Qin, and J. Hu, Magnetic switches via electric field in BN nanoribbons, Appl. Surf. Sci. **480**, 300 (2019).

[40] C. Zhang, L. Wang, Y. Gu, X. Zhang, X. Xia, S. Jiang, L. L. Huang, Y. Fu, C. Liu, J. Lin, *et al.*, Hard ferromagnetic behavior in atomically thin $CrSiTe_3$ flakes, Nanoscale **14**, 5851 (2022).

[41] H. Li, J. Wu, X. Huang, G. Lu, J. Yang, X. Lu, Q. Xiong, and H. Zhang, Rapid and reliable thickness identification of two-dimensional nanosheets using optical microscopy, ACS Nano **7**, 10344 (2013).

[42] Y. Li, Z. Chen, J. Wang, T. Li, M. Tian, J. Karel, and K. Suzuki, Abnormal thickness-dependent magneto-transport properties of vdW magnetic semiconductor $Cr_2Si_2Te_6$, npj 2D Mater. Appl. **7**, 39 (2023).

[43] J. Lu, O. Zheliuk, Q. Chen, I. Leermakers, N. E. Hussey, U. Zeitler, and J. Ye, Full superconducting dome of strong Ising protection in gated monolayer WS_2, Proc. Natl Acad. Sci. USA **115**, 3551 (2018).

[44] J. T. Ye, Y. J. Zhang, R. Akashi, M. S. Bahramy, R. Arita, and Y. Iwasa, Superconducting dome in a gate-tuned band insulator, Science **338**, 1193 (2012).

[45] J. Zhang, A. Yang, X. Wu, J. Van De Groep, P. Tang, S. Li, B. Liu, F. Shi, J. Wan, Q. Li, *et al.*, Reversible and selective ion intercalation through the top surface of few-layer MoS_2, Nat. Commun. **9**, 5289 (2018).

[46] X. Jiang, M. Qin, X. Wei, L. Xu, J. Ke, H. Zhu, R. Zhang, Z. Zhao, Q. Liang, Z. Wei, *et al.*, Interplay between superconductivity and the strange-metal state in FeSe, Nat. Phys. **19**, 365 (2023).

[47] N. Lu, P. Zhang, Q. Zhang, R. Qiao, Q. He, H. B. Li, Y. Wang, J. Guo, D. Zhang, Z. Duan, *et al.*, Electric-field control of tri-state phase transformation with a selective dual-ion switch, Nature (London) **546**, 124 (2017).

[48] W. Zhuo, B. Lei, S. Wu, F. Yu, C. Zhu, J. Cui, Z. Sun, D. Ma, M. Shi, H. Wang, *et al.*, Manipulating ferromagnetism in few-layered $Cr_2Ge_2Te_6$, Adv. Mater. **33**, 2008586 (2021).

[49] T. J. Williams, A. A. Aczel, M. D. Lumsden, S. E. Nagler, M. B. Stone, J. Q. Yan, and D. Mandrus, Magnetic correlations in the quasi-two-dimensional semiconducting ferromagnet $CrSiTe_3$, Phys. Rev. B **92**, 144404 (2015).

[50] J. H. Park, S. W. Cheong, and C. T. Chen, Double-exchange ferromagnetism in $La(Mn_{1-x}Co_x)O_3$, Phys. Rev. B **55**, 11072 (1997).

[51] Z. L. Liao, G. Koster, M. Huijben, and G. Rijnders, Experimental evidence for anisotropic double exchange interaction driven anisotropic transport in manganite heterostructures, Sci. Rep. **7**, 2654 (2017).